



Mechanisms driving high-cycle fatigue life of as-built Inconel 718 processed by laser powder bed fusion

Dillon S. Watring^a, Kristen C. Carter^a, Dustin Crouse^b, Bart Raeymaekers^a, Ashley D. Spear^{a,*}

^a Department of Mechanical Engineering, University of Utah, Salt Lake City, UT, USA

^b Metals Customer Innovation Center, 3D Systems, Littleton, CO, USA

ARTICLE INFO

Keywords:

Additive manufacturing
Laser powder bed fusion
Inconel 718
High-cycle fatigue life
Fractography
Surface roughness

ABSTRACT

This study investigates the relationships among the high-cycle fatigue life, surface roughness, and additive manufacturing processing parameters in laser powder bed fusion Inconel 718 in the as-built condition. Standardized fatigue specimens were manufactured using 25 different sets of processing parameters by varying laser power, scan speed, layer thickness, and build orientation, with three repeat specimens per parameter set. Surface roughness measurements were conducted using white light interferometry; high-cycle fatigue life was measured; and fractography analysis was performed using scanning electron microscopy. Two processing-parameter metrics were observed to dominate high-cycle fatigue life: build orientation and laser-energy density. Build orientation affected fatigue life due to the relationship between build orientation and surface roughness. Increasing surface roughness decreased the fatigue life due to increasing number of surface-crack initiation sites. For a fixed build orientation, the laser-energy density, outside of the optimal range, decreased the fatigue life due to sub-surface defects. Specifically, fractography analysis showed that sub-surface defects consisted of lack-of-fusion pores at low laser-energy densities and secondary cracking and pores (possibly related to keyholing) at high laser-energy densities. While variability in residual stresses among the specimens could also play a role, this work focuses on geometrical surface and sub-surface defects caused by different processing parameters and their corresponding impact on total fatigue life. Based on these findings, guidelines are offered to improve fatigue life of additively manufactured Inconel 718 in the as-built, non-heat-treated condition.

1. Introduction

While additive manufacturing (AM) has become a popular tool in a variety of different industries [1,2], there remain many unknowns regarding the relationships between the build or process parameters and the corresponding quality, reliability, and the performance of the parts [3]. There are many different AM techniques used to manufacture metal parts. These techniques are typically categorized as powder bed fusion (PBF) and direct energy deposition (DED) [4]. Powder bed fusion can be separated further into laser powder bed fusion (L-PBF) [5] and electron beam melting (EBM) [6]. In L-PBF, metal powder is spread or rolled onto a build plate. A scanning laser is then used to locally melt/fuse a thin layer of metal powder to create the first layer. This is repeated layer-by-layer, until the full three-dimensional part is completed. L-PBF has many benefits over traditional manufacturing and other metal AM techniques, including high accuracy in fine details, near net-shape production of complex geometries, and the ability to use a variety of metals and their alloys [7], including Inconel.

Inconel is a nickel-based superalloy that has become increasingly popular in the aerospace, nuclear, and marine industries, due in part to its ability to retain its strength over a wide temperature range. Particularly, Inconel shows excellent mechanical properties especially at high temperatures and in corrosive environments [8], whereas mechanical properties of aluminum and steels may degrade in such conditions [9–12]. Inconel creates a passivating oxide layer during heating, which prevents the surface from further heating and corrosion [13]. Additionally, Inconel shows an increase in strength due to solid solution and precipitation hardening [14]. One of the most commonly used Inconel alloys is 718 [15]. Inconel 718 (IN 718) shows many improved mechanical properties over other Inconel alloys. However, due to its high hardness and low thermal conductivity, it is significantly more difficult and costly to machine [16–19]. AM techniques have shown the ability to create near-net shaped parts, which could solve many of the concerns with IN 718 [20]. IN 718 manufactured by L-PBF methods has been shown to have similar mechanical properties to wrought 718 [21]. Wang et al. [21] showed that the tensile strength and ductility of

* Corresponding author.

E-mail address: ashley.spear@utah.edu (A.D. Spear).

<https://doi.org/10.1016/j.msea.2019.06.003>

Received 23 April 2019; Received in revised form 31 May 2019; Accepted 2 June 2019

Available online 05 June 2019

0921-5093/ © 2019 Elsevier B.V. All rights reserved.

selective laser melted (SLM¹) IN 718, which was solution treated and double aged, were comparable to those of wrought 718. Specifically, they observed an ultimate tensile strength range of 1137–1358 MPa for SLM IN 718 compared to 1200–1400 MPa for wrought 718 and observed an almost identical elastic modulus of 201 GPa versus 208 GPa. However, Hilaire et al. [22] showed the influence of varying processing parameters on the microstructure, yield strength, and ultimate strength of L-PBF IN 718 and concluded that the optimization of processing parameters should be performed to maximize the mechanical properties. Although L-PBF IN 718 has similar mechanical properties to those of wrought 718, the fatigue life of L-PBF IN 718 has been shown to be significantly lower than that of wrought 718 [23]. Specifically, Gribbin et al. [24] showed that the decrease in low-cycle fatigue life of heat-treated (solution treated and double aged), direct metal laser sintered (DMLS²) IN 718 was due to the presence of porosity. Additionally, others have shown that porosity in heat-treated L-PBF IN 718 parts can be induced by varying processing parameters [25]. Thus, a thorough understanding and control of the processing parameters are required for optimizing the fatigue life in L-PBF IN 718.

The objective of this study was to examine the relationships among the AM process parameters (laser power, laser scan speed, layer thickness, and build orientation), surface roughness parameters, and high-cycle fatigue life of as-built L-PBF IN 718. Few studies exist in the open literature that have investigated this particular material in the as-built condition, without applying heat treatments or stress relieving. However, there are potential applications, such as deployment of AM machines in the field, where it may not be possible to perform heat treatments. Thus, to optimize AM parts for use in such applications, there is a need to better understand the process-property relationships for the as-built condition. Therefore, the L-PBF specimens in this work had no heat treatments applied (e.g., stress relief, solution treatment, double aging, etc.). A total of 11 different laser powers, 13 different laser scan speeds, two different layer thicknesses, and three different build orientations were investigated. The high-cycle fatigue life for different combinations of AM processing parameters was determined, and the competing mechanisms driving the fatigue life of L-PBF IN 718 were investigated.

2. Methods and materials

2.1. Materials and processing parameters

The test specimens used in this study were fabricated from 3D Systems IN 718 powder, which was recycled powder within 3D Systems useable standards. Analysis of the particle-size and aspect-ratio distributions of the IN 718 powder was performed in accordance with the ASTM F1877 standard [26]. Standardized fatigue test specimens were manufactured with a target gauge width of 6.36 mm and target gauge thickness of 3.10 mm, in accordance with the ASTM E466-15 standard [27]. Fig. 1a shows the target dimensions of the specimens. The specimens were built using 3D Systems ProX DMP 320 machine. In total, 25 different parameter sets were defined, each having a unique combination of laser power, laser scan speed, layer thickness and build orientation. The upper and lower values for the laser power and laser scan speed were selected based on the manufacturer's specified limits. The laser power ranged from 115 W to 465 W, with 11 different values selected within that range, and the laser scan speed ranged from 620 mm/s to 1770 mm/s, with 13 incremental values selected. The values for the layer thickness were set to the ProX DMP 320 standard thicknesses: 30 μm and 60 μm . Each specimen was manufactured such that the loading axis was aligned 0°, 60°, or 90° relative to the recoater

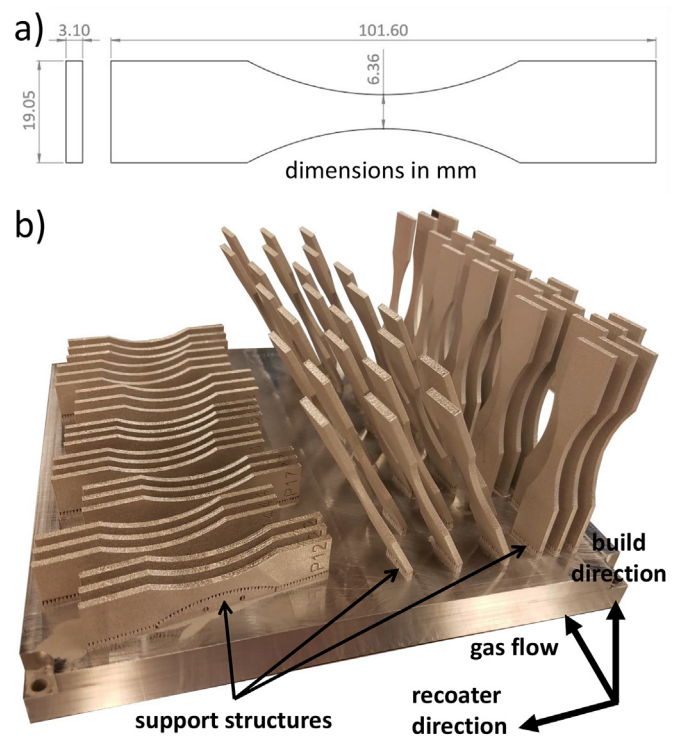


Fig. 1. a) Specimen dimensions in accordance with ASTM E466-15. b) All as-built IN 718 specimens on the build plate prior to removal with support structures shown.

direction in the build plate, as shown in Fig. 1b. For the purpose of this study, the hatch spacing and spot size were held constant at standard values: 100 μm and 50 μm , respectively. The entire parameter matrix can be seen in Table 1. Additionally, all of the 30 μm thickness specimens were built using contouring parameters of 115 W and 625 mm/s for the laser power and scan speed; whereas, the 60 μm thickness specimens were built using 165 W and 625 mm/s contouring parameters. The parameter ranges were chosen such that volumetric laser-energy density (E_p) ranged from approximately 30 to 90 J/mm³, based on optimal values specified by 3D Systems. The volumetric laser-energy density is $E_p = \frac{P}{vht}$, where P is the laser power, v is the scan speed, h is the hatch spacing, and t is the layer thickness [28]. For each parameter set, there were three fatigue specimens manufactured, for a total of 75 specimens. All of the specimens were tested in the as-built condition (i.e., no post-processing or secondary heat-treatments were performed).

2.2. Surface roughness measurements

Surface roughness was measured in the gauge region for all 75 specimens. The surface roughness measurements were obtained using a Zeta 3D optical profilometer with a 10 \times objective lens. Three scans per side on all four sides of the gauge region were measured covering an area of 948 μm by 711 μm . Ten different surface roughness metrics were quantified for each specimen, namely Ra, Rms, Rt, Rsk, Rku, RzDIN, RzJIS, η , ρ , and σ_s . A description of all of the surface roughness parameters is provided in Appendix A.

2.3. Fatigue testing

Following surface roughness measurements, all 75 specimens were cyclically loaded (tension-tension) to failure with a maximum stress of 600 MPa, stress ratio of 0.1, and a frequency of 20 Hz. The fatigue testing parameters were chosen such that the total fatigue-life testing was in the high-cycle range (i.e. within the elastic regime) at a fixed

¹ Selective laser melting (SLM) is a commonly used L-PBF technique.

² Direct metal laser sintering (DMLS) is another commonly used L-PBF technique.

Table 1

Test matrix for L-PBF IN 718 processing parameter sets. For each parameter set, three specimens were manufactured and tested.

Parameter	Power	Scan speed	Layer thickness	Build orientation	Laser-energy density
set	(W)	(mm/s)	(μm)	($^{\circ}$)	(J/mm^3)
1	220	1180	30	60	62.15
2	330	1770	30	0	62.15
3	115	620	30	90	61.83
4	168	1475	30	0	37.97
5	275	1200	30	0	76.39
6	115	915	30	60	41.89
7	330	1475	30	60	74.58
8	168	1180	30	90	47.46
9	200	800	30	90	83.33
10	275	1770	30	60	51.79
11	315	1050	60	60	50.00
12	465	1450	60	0	53.45
13	240	850	60	90	47.06
14	165	850	60	0	32.35
15	390	1050	60	60	61.90
16	465	1400	60	90	55.36
17	165	650	60	0	42.31
18	240	1250	60	60	32.00
19	315	1250	60	60	42.00
20	390	1450	60	90	44.83
21	220	1180	30	0	62.15
22	220	1180	30	90	62.15
23	315	1050	60	0	50.00
24	315	1050	60	90	50.00
25	200	1000	60	90	33.33

stress amplitude, which would result in fatigue failure within a tractable number of cycles (nominally 100,000). To that end, the stress amplitude was identified using S–N curves (at $R = 0.1$) from the literature for AM IN 718 [23]. Note that the reported yield strength of L-PBF IN 718 is between 800 MPa and 1100 MPa [29,30], which is well above the applied peak stress. The fatigue testing was performed in force control at a frequency of 20 Hz on an MTS 810 servo-hydraulic testing machine using a 25 kN load cell. Hydraulic grips were used to hold the specimens at 20 MPa, which is approximately 3.3% of the maximum applied stress. The cross-sectional area of each specimen was measured using a Keyence VHX-5000 optical microscope, which was then used to accurately determine the load required to reach a maximum applied stress of 600 MPa.

2.4. Fractography

Fractography analysis was performed on each specimen after fatigue failure using a Hitachi S–2600 N scanning electron microscope (SEM). Representative images for specimens with the same laser-energy density but different build orientations were analyzed to quantify the amount of fracture initiation beginning on the surfaces of the specimens. Additionally, representative images for specimens with different laser-energy densities but the same build orientation were analyzed to investigate the sub-surface defects.

3. Results

3.1. Powder characterization

Fig. 2 shows SEM images of the IN 718 powder at low and high magnification. The majority of the powder particles are spherical or near spherical (similar to Fig. 2b). However, some particles appeared to be partially fused (Fig. 2c) and display an oblong morphology (Fig. 2d). SEM images similar to that shown in Fig. 2a were used to determine the powder particle-size distribution for a population of 534 particles, shown in Fig. 3, which is similar to those seen in the literature [21]. The

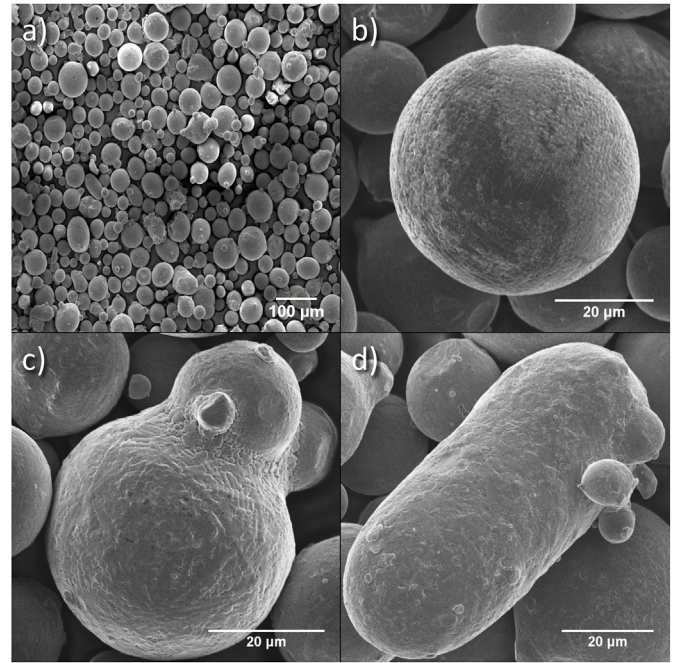


Fig. 2. Representative SEM images of IN 718 powder particles showing a) an overview, b) perfectly spherical particles, c) partially fused particles, and d) oblong shaped particles.

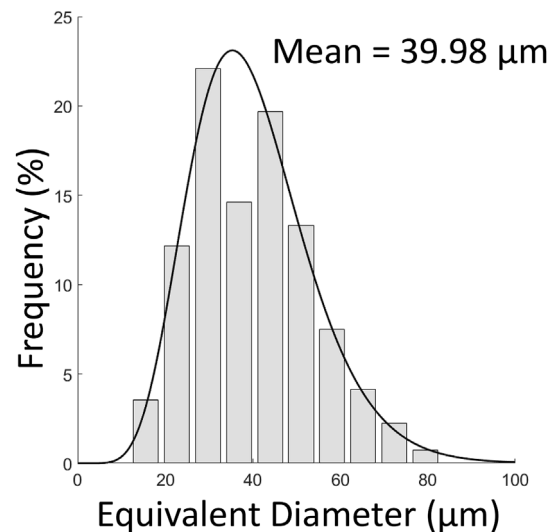


Fig. 3. Inconel 718 powder particle size distribution determined using SEM particle mapping.

mean particle size was found to be 39.98 μm , compared to 43.8 μm reported by 3D Systems.

3.2. Surface roughness

A correlation study was performed to determine the roughness parameters exhibiting the strongest correlation to the high-cycle fatigue life. The methodology and results from the correlation study are presented in Appendix B. The average of three scans was taken for each side, and the maximum of the averaged values among the four sides was used to represent the overall roughness for a given specimen. Based on results from the correlation analysis, it was found that no one parameter correlated with high-cycle fatigue life significantly more than the other parameters. Therefore, to simplify the presentation of results,

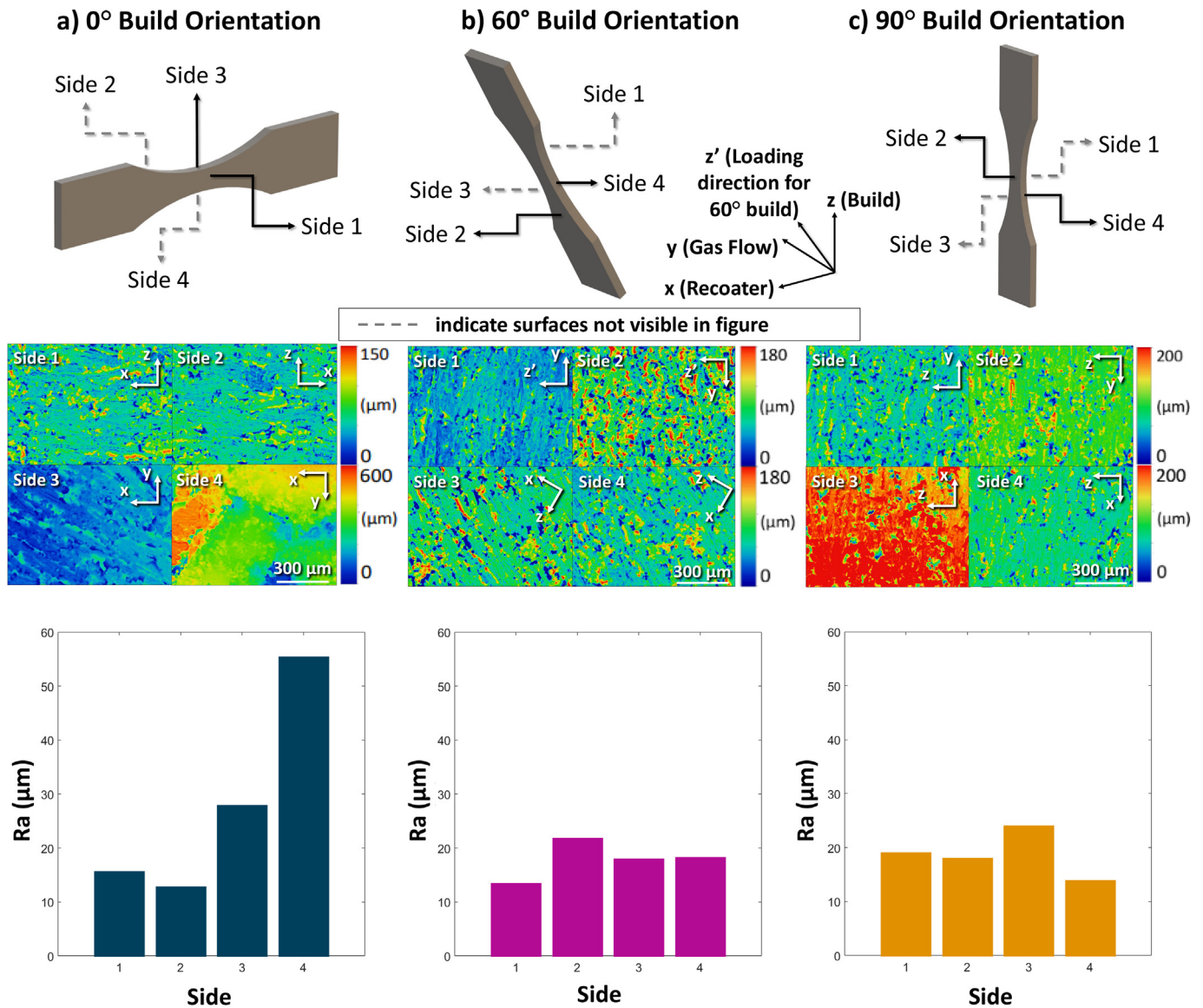


Fig. 4. Representative surface topography maps and Ra values for a) 0° build orientation, b) 60° build orientation, and c) 90° build orientation. Note, contour limits for the maps are scaled differently to enable visual contrast for each surface.

only the average roughness value (Ra) will be considered and discussed. Fig. 4 shows representative surface topography maps of each side of the specimens for each of the build orientations. For the 0° build orientation, the surface topography maps for sides three and four have been plotted using a different scale than that for sides one and two due to the significant difference in surface-roughness magnitude. The significantly higher surface roughness for side four in the 0° build orientation specimen is likely due to the supports that were needed during the printing process (see Fig. 1b). The 90° build orientation specimens showed the next roughest surfaces, with side three being the roughest (Fig. 4c). It can be postulated that this difference in surface roughness (between sides three and four) could be caused by some mechanism attributed to the gas flow direction. The surface roughness of the 60° build orientation specimens was slightly less than the 90° specimens, with the roughest side being side two, which can be attributed to the downskin of the specimen.

3.3. Fatigue life

Fig. 5 shows the fatigue life as a function of the different sets of process parameters, by comparing the total fatigue life to the

volumetric laser-energy density for different layer thickness and build orientation. For a fixed build orientation, the total fatigue life presented in Fig. 5a exhibits a bell-shaped relationship with respect to the laser-energy densities, which tend to result in lower total fatigue life for lower and higher laser-energy densities. Fig. 5b shows a similar trend, although it is less pronounced. It is noted that one specimen for the 60 μm, 90° build orientation, and lowest energy density showed visual signs of damage prior to loading. Namely, it showed significant warping, which could be due to residual stresses from the manufacturing process, and notches on the edges, which could be due to removing the support structures. Therefore, it was considered an outlier and was not included in the trend line shown for that data set. Overall, the specimens built at a 60° build orientation with a laser-energy density of 62.15 J/mm³ and 30 μm thickness resulted in the maximum total fatigue life among all parameter sets considered in this study.

3.4. Fractography

Fig. 6 shows the fracture surfaces of nine test specimens selected from 30 μm layer thickness at three different laser-energy densities from each build orientation: 45 J/mm³, 62 J/mm³, and 77 J/mm³. The

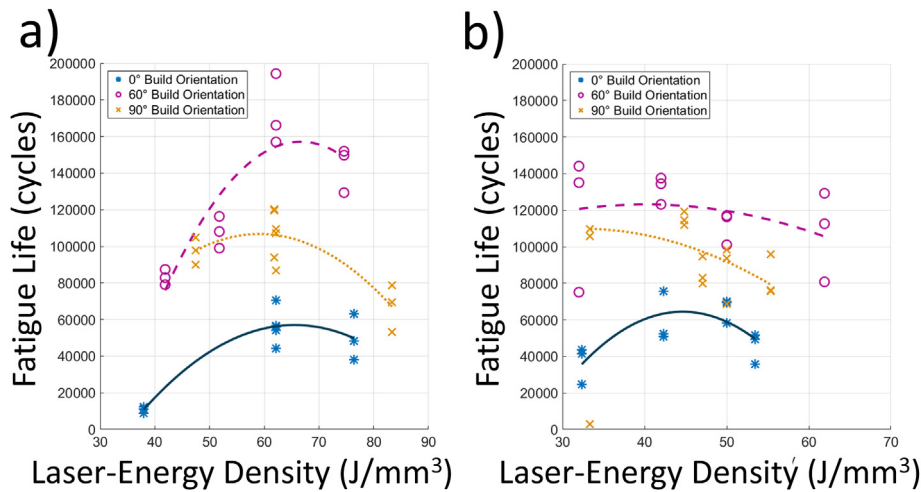


Fig. 5. High-cycle fatigue life versus volumetric laser-energy density for a) 30 μm layer thickness specimens and b) 60 μm layer thickness specimens.

middle column corresponds to specimens displaying the highest total fatigue life (62 J/mm³ laser-energy density). In the first column (45 J/mm³), there is consistently a very tortuous fracture surface compared to the other laser-energy densities, which is indicative of a high amount of porosity or defects. Fig. 7 shows higher magnification images that revealed the majority of these defects consisted of lack-of-fusion pores with powder particles present. Additionally, Fig. 7 shows a significant amount of secondary cracking and pores at high laser-energy densities. Fig. 8 shows lower magnification images displaying the transition from stable crack growth to final fracture. The relative portion of stable crack-growth area per cross section is approximately 49.25% for the 0° specimen, 76.71% for the 60° specimens, and 52.58% of the 90°

specimens. Similar trends were observed in the 60 μm layer thickness specimens.

The main difference among the three build orientations was the number of crack initiation sites observed on the specimen surfaces. Surface-crack initiation sites were observed in all three specimens; however, there were significantly more surface-crack initiation sites observed in the 0° build orientation specimens, fewer in the 90° specimens, and the fewest in the 60° specimens. Fig. 9 shows representative images of surface-crack initiation sites. Surface-crack initiation predominantly occurred on sides three and four, which corresponded to the roughest surfaces. There were approximately 63% more occurrences of surface-crack initiation sites for the 0° specimens compared to

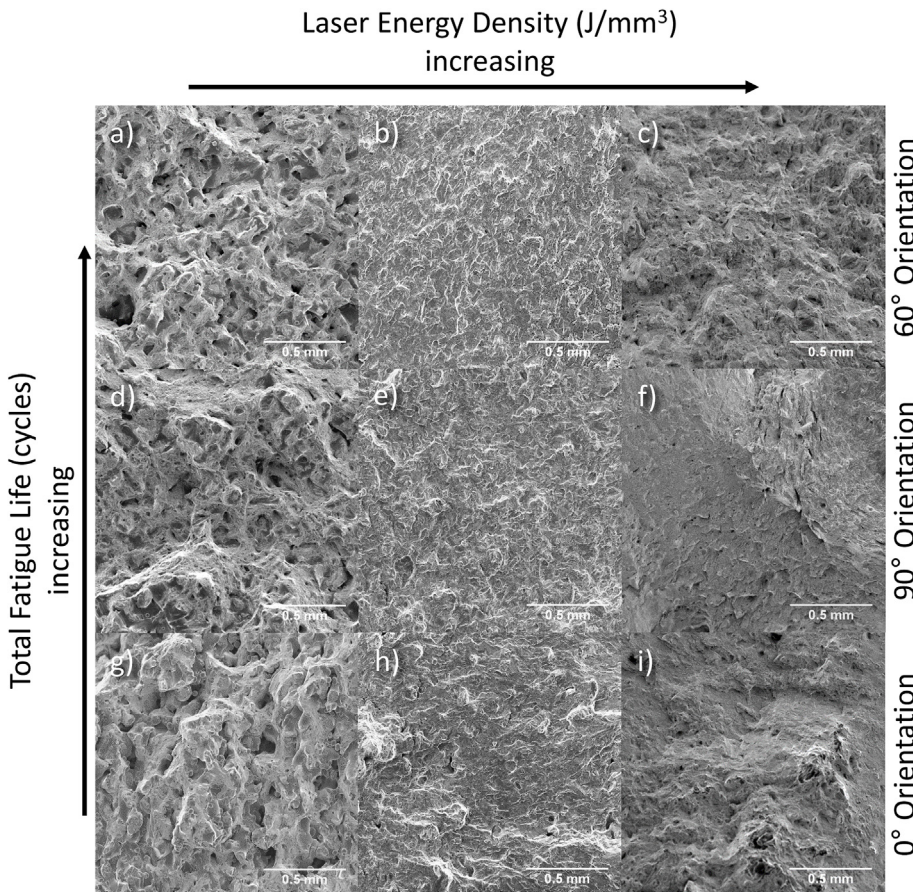


Fig. 6. SEM images of fracture surfaces of high-cycle fatigue-tested L-PBF IN 718 for 30 μm build-layer thickness at a) 45 J/mm³ and 60° build orientation, b) 62 J/mm³ and 60° build orientation, c) 77 J/mm³ and 60° build orientation, d) 45 J/mm³ and 90° build orientation, e) 62 J/mm³ and 90° build orientation, f) 77 J/mm³ and 90° build orientation, g) 45 J/mm³ and 0° build orientation, h) 62 J/mm³ and 0° build orientation, i) 72 J/mm³ and 0° build orientation.

Low energy densities

High energy densities

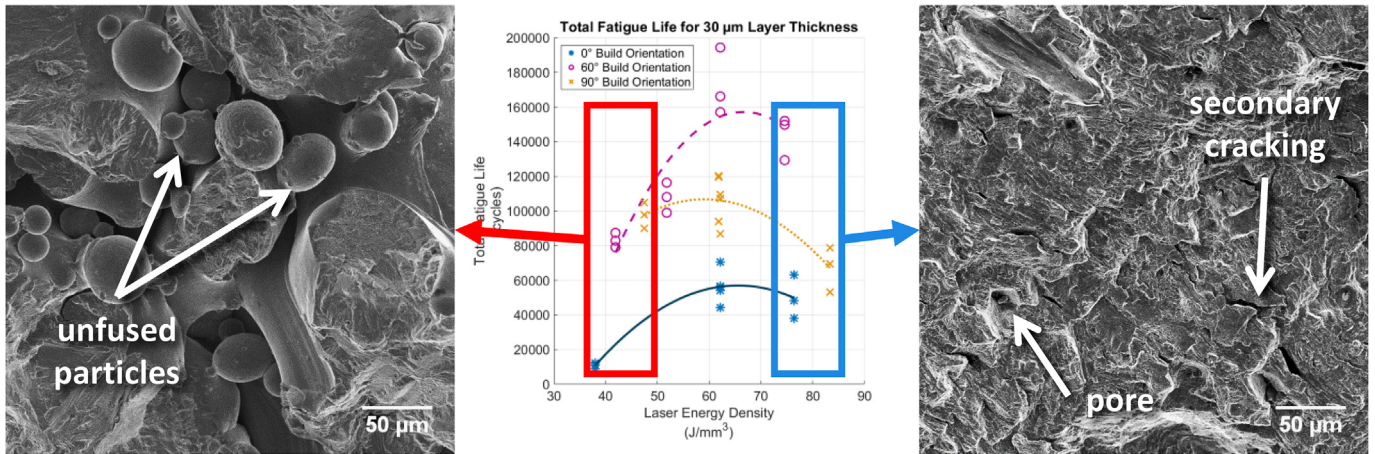


Fig. 7. High-cycle fatigue life dependence on sub-surface defects.

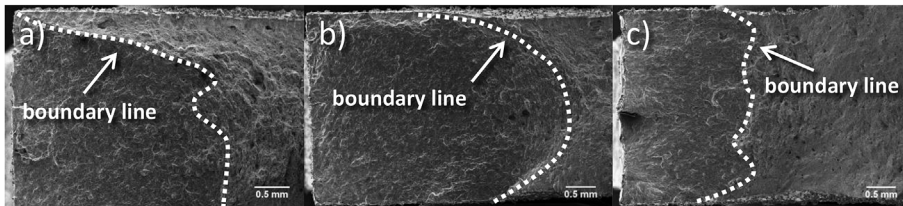


Fig. 8. Representative SEM images of fracture surfaces showing stable crack growth (left of the boundary line) and final fracture region (right of the boundary line) for 30 μm layer thickness: a) 0° specimen with $N_f = 70523$ cycles, b) 60° specimen with $N_f = 194329$ cycles, and c) 90° specimen with $N_f = 120255$ cycles.

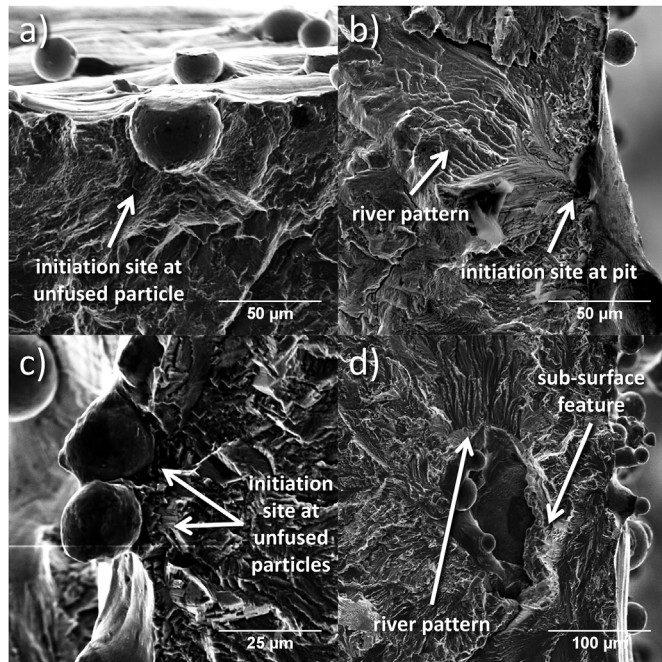


Fig. 9. Representative SEM images of surface cracks for a) 60° specimens, b) 90° specimens, c) 0° specimens, and d) a representative sub-surface initiation site.

the 60° specimens and approximately 29% more in the 90° specimens compared to the 60° specimens (all for the 30 μm layer thickness). Table 2 shows the number of surface-crack initiation sites observed on the surface of each specimen.

4. Discussion

To facilitate the use of L-PBF IN 718 in fatigue critical applications, it is paramount to understand the mechanisms that determine the fatigue life of L-PBF IN 718. In this work, two different relationships were observed: the relationship between surface roughness and high-cycle fatigue life, and the relationship between laser-energy density and high-cycle fatigue life.

4.1. Relationship between build orientation, surface roughness, and high-cycle fatigue life

The results from sections 3.2 and 3.3 are synthesized in Fig. 10, which shows the maximum surface roughness, the high-cycle fatigue life, and build orientation for each specimen. It is evident that fatigue life is dependent upon surface roughness, which is dependent upon the build orientation. The 0° build orientation exhibits rougher surfaces and generally results in lower fatigue life. On the other hand, the 60° build orientation, which Fig. 5 shows to provide the highest values of fatigue life, exhibits low surface roughness. While increasing surface roughness is generally regarded to decrease fatigue life, a question of interest is whether stress concentrations associated with AM-induced surface roughness increases the number of crack initiation sites, or whether the number of crack initiation sites is approximately the same but have earlier onsets. To investigate this, the fracture surfaces were carefully analyzed. The 0° build orientation specimens showed significantly more surface-crack initiation sites; whereas, for the surfaces with lower roughness values, fewer surface-crack initiation sites existed. Fig. 8 shows overviews of representative surfaces of the three different build orientations at identical laser-energy densities. There were

Table 2

Number of observed surface-crack initiation sites from one representative sample at each build orientation.

Build orientation	Medium laser-energy density
0°	57
60°	35
90°	45

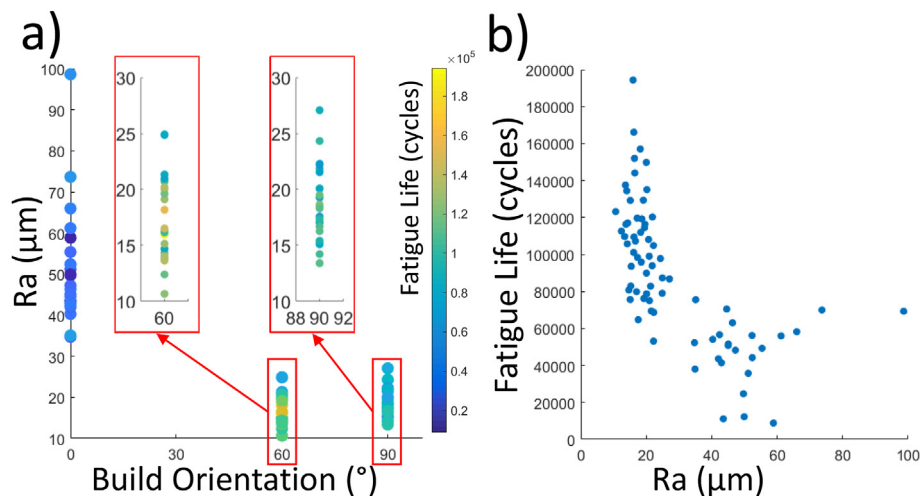


Fig. 10. a) Relationship among high-cycle fatigue life, roughness average parameter (Ra), and the build orientation for all three build orientations ($n = 75$ samples). Magnified views are shown for 60° and 90° build orientations. b) Relationship between the high-cycle fatigue life and Ra for all 75 samples.

approximately 60% more crack initiation sites on the surfaces for the 0° build orientation compared to the 60° build orientation for the 30 μm layer thickness. Others have demonstrated that multiple initiation sites lead to higher crack driving forces [31–34], which can lead to increased crack growth rates. The 0° build orientation had the lowest high-cycle fatigue life and the highest number of surface cracks. Therefore, it can be inferred that the number of crack initiation sites impacts the crack growth rates, reducing the number of cycles to reach fracture (propagation cycles). Additionally, it can be postulated that some of the reduction in fatigue life could be due to early onset of crack initiation. Spear et al. [35] have shown that early initiation of fatigue cracks can be caused by local, pit-induced, stress concentrations. The reduction of fatigue life in the specimens with higher surface roughness can hence be attributed to a reduction in the propagation cycles due to a larger number of crack initiation sites and a reduction in the cycles to initiation due to local stress concentrations on the surface.

Other work has been performed investigating the surface roughness and fatigue life of L-PBF IN 718. In work by Gockel et al. [36], the build orientation was held constant while varying contour power and scan speed of the fatigue specimens. They showed limited correlation between surface roughness (Ra) and fatigue life, which they attributed to powder particles on the surface that essentially obfuscate the underlying, more important, surface features. While Gockel et al. show that parameters like Ra might not adequately characterize fatigue-critical surface features, the results from this work suggest that Ra, nonetheless, exhibits meaningful correlation with fatigue life for the ranges of specimens studied here. One reason for this could be the variability of surface roughness that is introduced by varying build orientation, which has a clear impact on fatigue life. That is, due to significant variation of Ra values across all 75 specimens, the correlation coefficients with fatigue life are relatively high. Based on work by Gockel et al., it appears that using a more accurate description of relevant surface structure would lead to even stronger correlation coefficients. Testing this would require the use of X-ray computed tomography, which is beyond the scope of the current study; additionally, the overall trends presented in this work are not expected to vary by doing so.

Despite the clear trends among build orientation, surface roughness, and fatigue life, there does not appear to be a clear trend between surface roughness and fatigue life for a fixed build orientation (Fig. 10). This suggests that another mechanism must also play a role in the high-cycle fatigue life of L-PBF IN 718. To investigate the mechanism behind this variation, an analysis of the sub-surface defects was performed.

4.2. Relationship between laser-energy density and high-cycle fatigue life

From sections 3.3 and 3.4, it is evident that for a fixed build orientation, fatigue life is strongly dependent on sub-surface defect structure, which is, in turn, dependent upon volumetric laser-energy density. Sheridan et al. [25] have shown that for machined L-PBF IN 718 parts, the porosity can be induced by varying the processing parameters, which ultimately determines the fatigue life. The parameters that Sheridan et al. investigated were the power, velocity, hatch spacing, and layer thickness, which directly relate to the laser-energy density, for two different machines (Concept laser M2 cusing and EOS M290); however, a large range of laser-energy density was not investigated (only one value for the M2 and three values for the EOS M290). Furthermore, the relationship between the volumetric laser-energy density and the high-cycle fatigue life is more complicated than the relationship between the surface roughness and fatigue life. A bell-shaped curve relates the fatigue life to laser-energy density. A similar curve was observed in previous work when comparing porosity and laser-energy density [37,38]. Kantzos et al. [39] have shown that the introduction of porosity due to varying processing parameters reduces the fatigue life. For this specific AM process, an optimal range of volumetric laser-energy density exists, where the sub-surface defects (secondary cracking, porosity) are minimized, and the high-cycle fatigue life is maximized. The optimal range was around 60–70 J/mm³ and 40–45 J/mm³ for the 30 μm and 60 μm layer thickness specimens, respectively. At lower values of laser-energy density, the high-cycle fatigue life is significantly reduced. Similarly, the high-cycle fatigue life is significantly reduced at higher laser-energy densities.

The fractography analysis shows that in the low laser-energy density ranges, there was a very tortuous fracture surface indicative of a high amount of porosity. The porosity and sub-surface defects in the low energy density ranges are predominantly due to lack-of-fusion pores (Fig. 7). Typically, three to five Inconel particles were present in these lack-of-fusion pores, but fracture initiation was observed to begin at larger clusters of particles. However, the fractography analysis for the high laser-energy density specimens showed different sub-surface defects than the low laser-energy density specimens. There was a significant amount of secondary cracking observed (seen in Fig. 7) along with fracture initiating at sub-surface porosity. This could be due to keyhole (or other metallurgical) pores [40]. The secondary cracking observed could be due to a mechanism similar to hot cracking [41], hot tearing [42], or liquation cracking [43]. Hot cracking is caused by a high grain misorientation and hot tearing is caused by high residual stresses due to high temperature gradients. Chen et al. [43] concluded

that liquation cracking in AM IN 718 is due to the liquation of Laves/particles during manufacturing. They also observed that an increase in the heat input, due to processing parameters, resulted in an increase in susceptibility to liquation cracking, which can be compared to the increase in cracking observed in this work caused by an increase in the laser-energy density.

The fatigue behavior of L-PBF IN 718 presented in this study is consistent with literature showing that fatigue life in metals is typically driven by surface and sub-surface defects [44–47]. The main contribution of this work is the establishment of links among L-PBF build parameters and high-cycle fatigue life driving mechanisms, considering a broad space of build parameters. The mechanism of fracture initiation at surface defects is dominated by the surface roughness, which is predominantly governed by build orientation. For a given build orientation, the fatigue life is driven by the sub-surface defects in AM metals due to a high amount of lack-of-fusion pores at low laser-energy densities and metallurgical porosity at high laser-energy densities. The sub-surface defects are predominantly associated with the laser process parameters: laser power, scan speed, hatch spacing, and layer thickness. Although the results from the correlation analysis showed that no one parameter correlated with high-cycle fatigue life significantly more than the other parameters, it is expected that a non-line-of-sight measurement would result in even stronger correlation [36]. Additionally, there are other factors that could be affecting the overall correlation values in this work. Outside of the optimal range of laser-energy density, there is significant sub-surface porosity that may be reducing the surface-roughness correlation coefficients. A separate Pearson correlation analysis was performed among the fatigue life, Ra values, and Rms values using only the specimens in the optimal laser-energy density range. The results showed approximately a 33% increase in the magnitude of correlation coefficient for Ra (−0.571 to −0.763) and a 29% increase in the magnitude of correlation coefficient for Rms (−0.565 to −0.730). Additionally, the residual stresses due to the different laser-energy densities and build orientations may have influenced the fatigue results, thereby further impacting the correlation coefficients. While it is noted that variability in residual stresses induced by the L-PBF process also likely contributes to variability in fatigue life, the work presented here focuses on geometrical surface and sub-surface defects induced by the L-PBF process and their corresponding impact on total fatigue life.

5. Conclusions

In this study, a systematic design of experiment was performed to investigate the relationships among process parameters, surface roughness, and the high-cycle fatigue life of L-PBF IN 718. Based on the experimental test results and subsequent fractography analysis, the following conclusions are made:

1. In the high-cycle fatigue life of L-PBF IN 718, there are two competing mechanisms that influence the fatigue life. The first mechanism is associated with the build orientation and its relationship to surface roughness. Non-optimal build orientations lead to increased surface roughness, causing an increase in the number of surface-crack initiation sites and corresponding reduction in the fatigue life. The second mechanism is associated with the volumetric laser-energy density, which, outside of an optimal range, causes an increase in sub-surface defects and corresponding reduction in

fatigue life.

2. Among the build orientations considered, the worst total fatigue life was observed for the 0° build orientation specimens, while the 60° build orientation specimens showed the highest total fatigue life. The fractography analysis showed significantly more surface-crack initiation sites on the 0° build orientation specimens than on the 90° and 60° build orientation specimens. Hence, the fatigue life is largely driven by the surface roughness. The surface roughness contributes to the number of fracture initiation locations on the surface of the specimen and is predominantly associated with the build orientation. The reduction in fatigue life is likely caused by early onset of crack initiation and faster crack propagation rates due to higher driving forces stemming from the increased number of surface cracks.
3. The total fatigue life within a specific build orientation follows a bell-shaped curve. There is an optimal laser-energy density, depending on the layer thickness, for the total fatigue life. For the 30 μm layer thickness, this value is around 60–70 J/mm³. For the 60 μm layer thickness, it is around 40–45 J/mm³. This is consistent with previous work showing that at low and high values of energy densities, there is an increased amount of sub-surface porosity and defects. The laser-energy density drives the amount of sub-surface pores and defects, which ultimately drives the total fatigue life within a given build orientation. At low volumetric laser-energy density ranges, the sub-surface defects consist of lack-of-fusion pores. At high volumetric laser-energy density ranges, the sub-surface defects consist of keyhole (or other metallurgical) pores and secondary cracking possibly caused by a hot-tearing-like mechanism.
4. Similar to traditional materials, the total fatigue life in AM Inconel 718 is dominated by surface and sub-surface defects. Residual stresses may also affect the high-cycle fatigue life but were not investigated in this work. From this work, however, the conclusion can be made that to maximize the total fatigue life of as-built L-PBF IN 718, the manufacturing process should minimize the sub-surface defects through process parameter optimization (specifically the laser power, scan speed, hatch spacing, and layer thickness) and also minimize the surface roughness through build orientation or machining when possible.

Data availability

The processed surface-roughness data and corresponding build parameters can be found on Citrination [<https://citrination.com/datasets/178858>]. The fatigue-life data cannot be shared at time of publication because the data are being used in an ongoing study.

Acknowledgements

This research is supported by the Department of Defense Office of Economic Adjustment (ST1605-19-03) and by the National Science Foundation under Grant No. CMMI-1752400. The authors would like to express gratitude to 3D Systems for supplying the materials; Jeff Kessler for assisting with mechanical testing; Brigham Young University Integrated Microfabrication Lab for providing access to the Zeta 20 3D Profilometer; and Drs. Nadia Kouraytem, Anthony Rollett, and Joy Gockel for the valuable discussions about this work.

Appendix A. Surface Roughness Parameters

Topography parameters considered in this work include the asperity-peak density (η), the asperity-peak radius (ρ), and the standard deviation of asperity-peak heights (σ_s). The spectral moment approach, developed by McCool et al. [48], was used to calculate the surface topography parameters. In this method, the topography parameters are calculated from the spectral moments m_0 , m_2 , and m_4 . However, this method accounts for a single, arbitrary cross section of the surface and can lead to significant variation of the calculated parameters depending on the cross section taken. A better approach to calculating the topography parameters, suggested by Pawar et al. [49], is to average the spectral moments from all cross sections and

then calculate the topography parameters from the averaged spectral moments. Additionally, the spectral moments can be affected by the finite difference discretization technique used. To be consistent with literature [50], the central finite difference discretization was used. The equations for calculating all of the surface roughness and topography parameters are presented in Table 3 below.

Table 3
Complete list of roughness and topography parameters investigated.

Description	Parameter
Roughness Average	Ra
Root Mean Squared	Rms (Rq)
Max Height of Profile	Rt
Skewness	Rsk
Kurtosis	Rku
Average Distance - Peak to Valley	RzDIN
Average Distance - Peak to Valley (Japanese Standard)	RzJIS
Asperity-Peak Density	η
Asperity-Peak Radius	ρ
Standard Deviation of Asperity-Peak Heights	σ_s

Surface roughness parameters:

$$R_a = \frac{1}{nm} \sum_{i=1}^n \sum_{j=1}^m Z_{ij} \quad (1)$$

$$R_{ms}(R_q) = \sqrt{\frac{1}{n} \frac{1}{m} \sum_{i=1}^n \sum_{j=1}^m Z_{ij}^2} \quad (2)$$

$$R_t = \max_{ij} Z_{ij} - \min_{ij} Z_{ij} \quad (3)$$

$$R_{sk} = \frac{1}{mnR_q^3} \sum_{i=1}^n \sum_{j=1}^m Z_{ij}^3 \quad (4)$$

$$R_{ku} = \frac{1}{mnR_q^4} \sum_{i=1}^n \sum_{j=1}^m Z_{ij}^4 \quad (5)$$

$$R_{zDIN} = \frac{1}{s} \sum_{i=1}^s R_{ti} \quad (6)$$

$$R_{zJIS} = \frac{1}{5} \sum_{i=1}^5 R_{ti} \quad (7)$$

$$\eta = \frac{m_4}{6\pi\sqrt{3}m_2} \quad (8)$$

$$\rho = 0.375 \sqrt{\frac{\pi}{m_4}} \quad (9)$$

$$\sigma_s = \sqrt{1 - \frac{0.8968}{\alpha}} \sqrt{m_0} \quad (10)$$

$$m_0 = AVG(Z^2) \quad (11)$$

$$m_2 = AVG\left(\left(\frac{dZ}{dx}\right)^2\right) \quad (12)$$

$$m_4 = AVG\left(\left(\frac{d^2Z}{dx^2}\right)^2\right) \quad (13)$$

$$\alpha = \frac{m_0 m_4}{m_2^2} \quad (14)$$

Appendix B. - Correlation Coefficients

Once all of the surface roughness and topography parameters were calculated, a correlation study was performed to determine the roughness parameters exhibiting the highest correlation to the high-cycle fatigue life. Three different correlation coefficients were investigated: the Pearson correlation, the distance correlation, and the Spearman correlation. The Pearson correlation coefficient measures the linear correlation between two variables [51]. The Spearman correlation measures the monotonic relationship between two variables, which can be linear or nonlinear [52].

Finally, the distance correlation measures both the linear and nonlinear relationship between two variables with one coefficient [53].

Pearson correlation coefficients (Fig. 11)

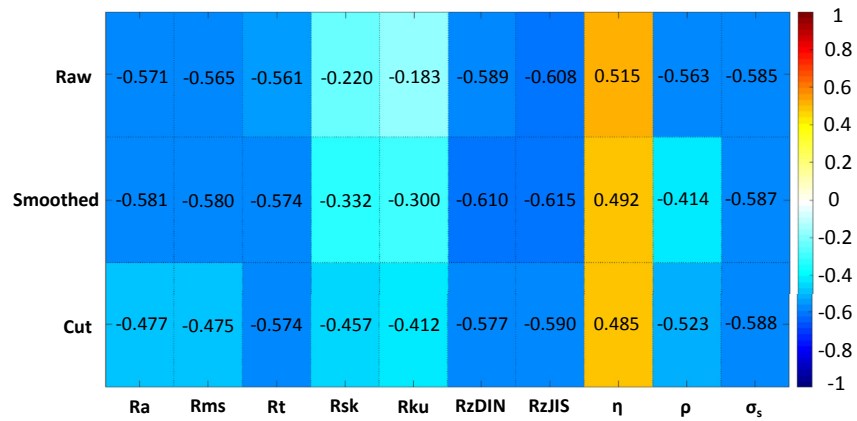


Fig. 11. Pearson correlation coefficient among surface roughness values and high-cycle fatigue life. The first row corresponds to raw profilometry data; the second row corresponds to profilometry data that have been smoothed using a standard mean filter; the third row corresponds to profilometry data where any height values greater or less than two standard deviations from the mean were considered outliers and therefore removed (cut) from the data set.):

$$r_{xy} = \frac{\sum_{i=1}^n (x_i - \bar{x})(y_i - \bar{y})}{\sqrt{\sum_{i=1}^n (x_i - \bar{x})^2} \sqrt{\sum_{i=1}^n (y_i - \bar{y})^2}} \tag{15}$$

Spearman correlation coefficients (Fig. 12)

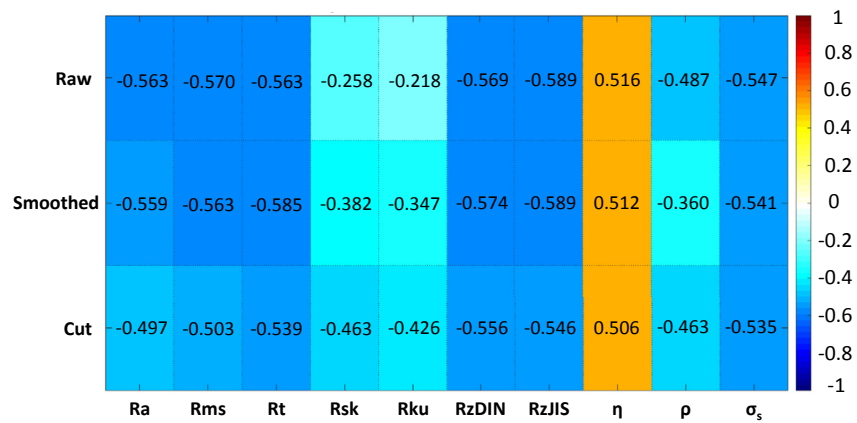


Fig. 12. Spearman correlation coefficient among surface roughness values and high-cycle fatigue life. The first row corresponds to raw profilometry data; the second row corresponds to profilometry data that have been smoothed using a standard mean filter; the third row corresponds to profilometry data where any height values greater or less than two standard deviations from the mean were considered outliers and therefore removed (cut) from the data set.):

$$r_s = 1 - \frac{6 \sum d_i^2}{n(n^2 - 1)} \tag{16}$$

$d_i = rg(X_i) - rg(Y_i)$, is the difference between ranks.

Distance correlation coefficients (Fig. 13)

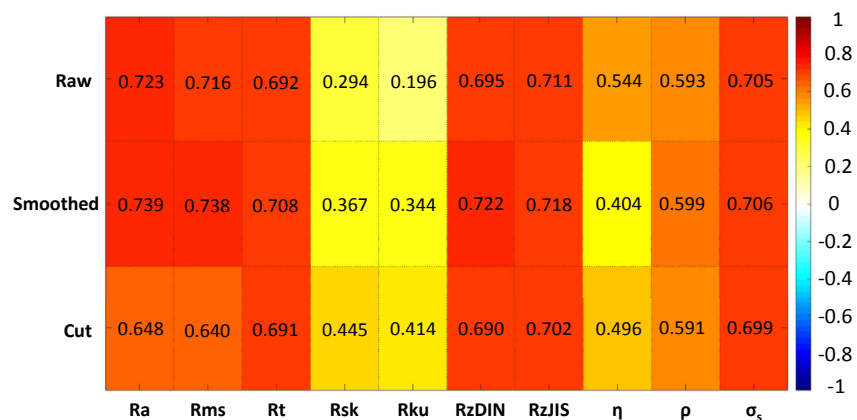


Fig. 13. Distance correlation coefficient among surface roughness values and high-cycle fatigue life. The first row corresponds to raw profilometry data; the second row corresponds to profilometry data that have been smoothed using a standard mean filter; the third row corresponds to profilometry data where any height values greater or less than two standard deviations from the mean were considered outliers and therefore removed (cut) from the data set.]:

$$dCor(X, Y) = \frac{dCov(X, Y)}{\sqrt{dVar(X)dVar(Y)}} \quad (17)$$

References

- [1] S.H. Huang, P. Liu, A. Mokasdar, L. Hou, Additive manufacturing and its societal impact: a literature review, *Int. J. Adv. Manuf. Technol.* 67 (5–8) (2013) 1191–1203.
- [2] B. Mueller, Additive manufacturing technologies—rapid prototyping to direct digital manufacturing, *Assemb. Autom.* 32 (2) (2012).
- [3] M. Schmidt, M. Merklein, D. Bourell, D. Dimitrov, T. Hausotte, K. Wegener, L. Overmeyer, F. Vollertsen, G.N. Levy, Laser based additive manufacturing in industry and academia, *CIRP Annals* 66 (2) (2017) 561–583.
- [4] N. Shamsaei, A. Yadollahi, L. Bian, S.M. Thompson, An overview of direct laser deposition for additive manufacturing; part ii: mechanical behavior, process parameter optimization and control, *Additive Manufacturing* 8 (2015) 12–35.
- [5] T.M. Mower, M.J. Long, Mechanical behavior of additive manufactured, powder-bed laser-fused materials, *Mater. Sci. Eng. A* 651 (2016) 198–213.
- [6] L.E. Murr, S.M. Gaytan, D.A. Ramirez, E. Martinez, J. Hernandez, K.N. Amato, P.W. Shindo, F.R. Medina, R.B. Wicker, Metal fabrication by additive manufacturing using laser and electron beam melting technologies, *J. Mater. Sci. Technol.* 28 (1) (2012) 1–14.
- [7] M. Baumers, Economic Aspects of Additive Manufacturing: Benefits, Costs and Energy Consumption, Ph.D. thesis © Martin Baumers, 2012.
- [8] E. Akca, A. Gürsel, A review on superalloys and IN718 nickel-based INCONEL superalloy, *Period. Eng. Nat. Sci.* 3 (1) (2015).
- [9] J. Warren, D. Wei, The cyclic fatigue behavior of direct age 718 at 149, 315, 454 and 538 °C, *Mater. Sci. Eng. A* 428 (1–2) (2006) 106–115.
- [10] A. Thomas, M. El-Wahabi, J. Cabrera, J. Prado, High temperature deformation of inconel 718, *J. Mater. Process. Technol.* 177 (1–3) (2006) 469–472.
- [11] K. Prasad, R. Sarkar, P. Ghosal, V. Kumar, M. Sundararaman, High temperature low cycle fatigue deformation behaviour of forged in 718 superalloy turbine disc, *Mater. Sci. Eng. A* 568 (2013) 239–245.
- [12] D.-H. Jeong, M.-J. Choi, M. Goto, H.-C. Lee, S. Kim, Effect of service exposure on fatigue crack propagation of inconel 718 turbine disc material at elevated temperatures, *Mater. Char.* 95 (2014) 232–244.
- [13] R. Molins, G. Hochstetter, J. Chassaing, E. Andrieu, Oxidation effects on the fatigue crack growth behaviour of alloy 718 at high temperature, *Acta Mater.* 45 (2) (1997) 663–674.
- [14] H. Zhang, S. Zhang, M. Cheng, Z. Li, Deformation characteristics of δ phase in the delta-processed inconel 718 alloy, *Mater. Char.* 61 (1) (2010) 49–53.
- [15] E. Ezugwu, Z. Wang, A. Machado, The machinability of nickel-based alloys: a review, *J. Mater. Process. Technol.* 86 (1–3) (1999) 1–16.
- [16] T. Sugihara, T. Enomoto, High speed machining of inconel 718 focusing on tool surface topography of cbn tool, *Procedia Manufacturing* 1 (2015) 675–682.
- [17] K. Rana, S. Rinaldi, S. Imbrogno, G. Rotella, D. Umbrello, R.M. Saoubi, S. Ayvar-Soberanis, 2d fe prediction of surface alteration of inconel 718 under machining condition, *Procedia CIRP* 45 (2016) 227–230.
- [18] J.-P. Costes, Y. Guillet, G. Poulachon, M. Dessoly, Tool-life and wear mechanisms of cbn tools in machining of inconel 718, *Int. J. Mach. Tool Manuf.* 47 (7–8) (2007) 1081–1087.
- [19] A.K. Parida, K. Maity, Comparison of the machinability of inconel 718, inconel 625 and monel 400 in hot turning operation, *Engineering Science and Technology, Int. J.* 21 (3) (2018) 364–370.
- [20] W.E. Frazier, Metal additive manufacturing: a review, *J. Mater. Eng. Perform.* 23 (6) (2014) 1917–1928.
- [21] Z. Wang, K. Guan, M. Gao, X. Li, X. Chen, X. Zeng, The microstructure and mechanical properties of deposited-in718 by selective laser melting, *J. Alloy. Comp.* 513 (2012) 518–523.
- [22] A. Hilaire, E. Andrieu, X. Wu, High-temperature mechanical properties of alloy 718 produced by laser powder bed fusion with different processing parameters, *Additive Manufacturing* 26 (2019) 147–160.
- [23] K. Morgan, Additive Manufacturing Overview: Propulsion Applications, Design for and Lessons Learned.
- [24] S. Gribbin, J. Bicknell, L. Jorgensen, I. Tsukrov, M. Knezevic, Low cycle fatigue behavior of direct metal laser sintered inconel alloy 718, *Int. J. Fatigue* 93 (2016) 156–167.
- [25] L. Sheridan, O.E. Scott-Emuakpor, T. George, J.E. Gockel, Relating porosity to fatigue failure in additively manufactured alloy 718, *Mater. Sci. Eng. A* 727 (2018) 170–176.
- [26] A. International, Standard Practice for Characterization of Particles, ASTM International.
- [27] A. International, Standard Practice for Conducting Force Controlled Constant Amplitude Axial Fatigue Tests of Metallic Materials, ASTM International.
- [28] J. Ciurana, L. Hernandez, J. Delgado, Energy density analysis on single tracks formed by selective laser melting with coormo powder material, *Int. J. Adv. Manuf. Technol.* 68 (5–8) (2013) 1103–1110.
- [29] K. Amato, S. Gaytan, L. Murr, E. Martinez, P. Shindo, J. Hernandez, S. Collins, F. Medina, Microstructures and mechanical behavior of inconel 718 fabricated by selective laser melting, *Acta Mater.* 60 (5) (2012) 2229–2239.
- [30] T. Trosch, J. Ströföner, R. Völkl, U. Glatzel, Microstructure and mechanical properties of selective laser melted inconel 718 compared to forging and casting, *Mater. Lett.* 164 (2016) 428–431.
- [31] K. Sadananda, A. Vasudevan, Short crack growth and internal stresses, *Int. J. Fatigue* 19 (93) (1997) 99–108.
- [32] K. Sadananda, A. Vasudevan, Crack tip driving forces and crack growth representation under fatigue, *Int. J. Fatigue* 26 (1) (2004) 39–47.
- [33] A. Mkaddem, M. El Mansori, On fatigue crack growth mechanisms of mmc: reflection on analysis of multi surface initiations, *Mater. Des.* 30 (9) (2009) 3518–3524.
- [34] H.J. Jin, S.J. Wu, A new driving force parameter for fatigue growth of multiple cracks, *Int. J. Fatigue* 96 (2017) 10–16.
- [35] A.D. Spear, A.R. Ingraffea, Effect of chemical milling on low-cycle fatigue behavior of an al–mg–si alloy, *Corros. Sci.* 68 (2013) 144–153.
- [36] J. Gockel, L. Sheridan, B. Koerper, B. Whip, The influence of additive manufacturing processing parameters on surface roughness and fatigue life, *Int. J. Fatigue* 124 (2019) 380–388.
- [37] E. Olakanmi, R. Cochrane, K. Dalgarno, Densification mechanism and microstructural evolution in selective laser sintering of al–12si powders, *J. Mater. Process. Technol.* 211 (1) (2011) 113–121.
- [38] T. Kimura, T. Nakamoto, Microstructures and mechanical properties of a356 (al–si7mg0.3) aluminum alloy fabricated by selective laser melting, *Mater. Des.* 89 (2016) 1294–1301.
- [39] C. Kantzos, J. Pauza, R. Cunningham, S.P. Narra, J. Beuth, A. Rollett, An investigation of process parameter modifications on additively manufactured inconel 718 parts, *J. Mater. Eng. Perform.* 28 (2) (2019) 620–626.
- [40] R. Cunningham, S.P. Narra, C. Montgomery, J. Beuth, A. Rollett, Synchrotron-based x-ray microtomography characterization of the effect of processing variables on porosity formation in laser powder-bed additive manufacturing of ti-6al-4v, *JOM (J. Occup. Med.)* 69 (3) (2017) 479–484.
- [41] Y. Chen, F. Lu, K. Zhang, P. Nie, S.R.E. Hosseini, K. Feng, Z. Li, Dendritic microstructure and hot cracking of laser additive manufactured inconel 718 under improved base cooling, *J. Alloy. Comp.* 670 (2016) 312–321.
- [42] C.E. Roberts, D. Bourell, T. Watt, J. Cohen, A novel processing approach for additive manufacturing of commercial aluminum alloys, *Physics Procedia* 83 (2016) 909–917.
- [43] Y. Chen, K. Zhang, J. Huang, S.R.E. Hosseini, Z. Li, Characterization of heat affected zone liquation cracking in laser additive manufacturing of inconel 718, *Mater. Des.* 90 (2016) 586–594.
- [44] K. Shiozawa, Y. Morii, S. Nishino, L. Lu, Subsurface crack initiation and propagation mechanism in high-strength steel in a very high cycle fatigue regime, *Int. J. Fatigue* 28 (11) (2006) 1521–1532.
- [45] G. Chai, The formation of subsurface non-defect fatigue crack origins, *Int. J. Fatigue* 28 (11) (2006) 1533–1539.
- [46] J. Hyzak, I. Bernstein, The effect of defects on the fatigue crack initiation process in two p/m superalloys: Part ii. surface-subsurface transition, *Metallurgical transactions A* 13 (1) (1982) 45–52.
- [47] A.D. Spear, S.F. Li, J.F. Lind, R.M. Suter, A.R. Ingraffea, Three-dimensional characterization of microstructurally small fatigue-crack evolution using quantitative fractography combined with post-mortem x-ray tomography and high-energy x-ray diffraction microscopy, *Acta Mater.* 76 (2014) 413–424.
- [48] J.I. McCool, Relating profile instrument measurements to the functional performance of rough surfaces, *J. Tribol.* 109 (2) (1987) 264–270.
- [49] G. Pawar, P. Pawlus, I. Etsion, B. Raeymaekers, The effect of determining topography parameters on analyzing elastic contact between isotropic rough surfaces, *J. Tribol.* 135 (1) (2013) 011401.
- [50] M. Kalin, A. Pogačnik, I. Etsion, B. Raeymaekers, Comparing surface topography parameters of rough surfaces obtained with spectral moments and deterministic methods, *Tribol. Int.* 93 (2016) 137–141.
- [51] K. Pearson, Determination of the coefficient of correlation, *Science* 30 (757) (1909) 23–25.
- [52] J.H. Zar, Significance testing of the spearman rank correlation coefficient, *J. Am. Stat. Assoc.* 67 (339) (1972) 578–580.
- [53] G.J. Székely, M.L. Rizzo, N.K. Bakirov, et al., Measuring and testing dependence by correlation of distances, *Ann. Stat.* 35 (6) (2007) 2769–2794.